small structures
www.small-structures.com

Advanced Multifunctional Oil Structurants for Sustainable Lubricants Engineered by Electrospinning Lignin/Cellulose Acetate Butyrate Nanofibers and TiO_2 Atomic Layer Deposition

*José F. Rubio-Valle, Eduardo Martínez-Guerra, Margarita Sánchez-Domínguez, Elisa Vázquez-Lepe, Ciro Rodríguez, Concepción Valencia, José E. Martín-Alfonso, and José M. Franco**

This work investigates the potential of electrospun nanofibers derived from alkaline kraft lignin (AKL) and cellulose acetate butyrate (CAB) as renewable structuring agents for vegetable oils and their modification with TiO_2 by means of atomic layer deposition (ALD). These nanofibers are targeted to replace the traditional components of lubricating greases with more ecofriendly multifunctional ingredients derived from renewable resources. The electrospinnability of AKL/CAB solutions improves with concentration, with a critical entanglement concentration ($C_e \approx 7.2$ wt%) that needs to be exceeded to obtain fiber-dominated nanostructures. Above C_e, increasing solution concentration yields larger fiber diameters (from 0.63 to 2.69 μm) and higher structural homogeneity. Higher CAB contents favor the formation of uniform nanofiber networks with improved elongational properties. Dispersions of AKL/CAB nanofiber mats in castor oil produce stable gel-like systems, with tunable rheological properties depending on nanofiber content and AKL:CAB ratio. Oleo-dispersions of AKL-rich nanofibers provide lower friction coefficients (≈0.11) and reduced wear (365 μm average scar diameter) in a tribological contact. ALD of TiO_2 on AKL/CAB nanofibers remarkably improves the tribological properties of these oleo-dispersions, significantly reducing friction (by 41%) and totally preventing wear, which is reported as a noticeable advance in the customization of renewable semisolid lubricants.

1. Introduction

In recent decades, there has been a clear policy trend toward sustainability and the management of renewable resources, which has played a critical role in combating climate change and promoting more equitable and resilient economic models.[1,2] These policies promote the use of renewable energy, sustainable agricultural practices, and the reuse of materials, not only protecting the environment but also driving economic growth and innovation.[3] Economies committed to sustainability and the management of renewable resources are also promoting innovation in the creation of new multifunctional materials and consumer goods.[4] Advanced materials and end-use formulations derived from renewable sources and eco-efficiently processed contribute to enhance a circular economy.[5,6] In the lubricant technology sector, it is estimated that ≈55% of the lubricants placed in the market ultimately contributes to environmental pollution.[7] This problem is exacerbated by the complex formulations of most lubricating greases, which consist of mineral or synthetic oils and nonbiodegradable and nonrenewable thickeners,

J. F. Rubio-Valle, C. Valencia, J. E. Martín-Alfonso, J. M. Franco
Pro2TecS—Chemical Product and Process Technology Research Center
Department of Chemical Engineering and Materials Science
ETSI
Universidad de Huelva
Campus de "El Carmen", 21071 Huelva, Spain
E-mail: franco@uhu.es

The ORCID identification number(s) for the author(s) of this article can be found under https://doi.org/10.1002/sstr.202500125.

DOI: 10.1002/sstr.202500125

E. Martínez-Guerra, M. Sánchez-Domínguez
Unidad Monterrey
Centro de Investigación en Materiales Avanzados, S.C. (CIMAV)
Alianza Norte 202, Apodaca 66628, Nuevo León, Mexico

E. Vázquez-Lepe, C. Rodríguez
Tecnológico de Monterrey
School of Engineering and Sciences
Ave. Eugenio Garza Sada 2501, Monterrey 64849, Nuevo León, Mexico

mainly metal soaps and polyureas, apart from packages of multiple functional additives.[8,9] Among the additives, some metal oxides, sulfides, graphite, and clays are often included to enhance lubricant performance, sometimes in the form of nanoparticles.[10–13] In recent years, the new trends in formulating lubricating greases have mainly focused either on improving the tribological performance through the use of more sophisticated additives,[14–16] or on making these formulations more sustainable and environmentally friendly,[17–19] as detailed later, or in both directions at the same time.[20,21]

Lubricant discharges, spills, or emissions during their service life pose significant environmental challenges, including water pollution, loss of biodiversity, depletion of natural resources, and waste generation.[22,23] To address these issues, a shift to more sustainable practices is essential in this industrial sector, including the development of fully renewable lubricants, effective waste management, and the adoption of cleaner technologies.

The functional properties of lubricating greases are largely influenced by the microstructure imparted by the thickener.[8] This component, typically composed of interwoven fibers, polymer chains, or other structural units, plays a critical role in the in-service performance and physical stability of the lubricant.[8] An effective strategy to reduce the environmental impact associated with traditional greases based on metal soaps or polyureas involves not only replacing mineral and synthetic oils with natural vegetable oils but also using biopolymers as thickeners in lubricating oils.[24,25] However, achieving the appropriate compatibility of these biopolymers with lubricating oils is challenging and often requires some form of chemical modification, such as acetylation,[26] methylation,[27] ethylation,[28] acylation,[29] or more complex functionalizations to[18,30] reduce the polarity of biopolymers and thus improve their performance and stability in lubricating oils. While the resulting formulations can be considered bio-based, inert, and nontoxic, many of these production processes involve relatively complex chemical reactions and, specially, the use of environmentally harmful chemicals and solvents.[31] One potential strategy to overcome these limitations is to promote the formation of gel-like dispersions through physical nanoscale interactions between biopolymer fibers and the oil phase.[32,33] The initial hypothesis is that a structure consisting of micro- or nano-sized fibers with high porosity and a substantial surface-to-volume ratio could induce the formation of a 3D percolation network within the oily medium.[34,35]

In the field of nanofabrication, electrospinning stands out from other techniques such as force spinning, melt spinning, and temperature-induced phase separation because of its industrial scalability and greater technological development.[36,37] Crucially, it is possible to tailor the morphology of electrospun fibers by adjusting the physicochemical properties of the feeding solution and operating parameters.[38,39] In addition, it integrates well with other techniques such as atomic layer deposition (ALD), offering unique opportunities to produce advanced materials at the nanometer scale.[40] In this synergy, electrospun fibers serve as a porous matrix, while ALD enables precise and selective surface modification.[41] From a fundamental standpoint, surface structure and flexibility are key factors in achieving high efficiency across various applications, including catalysis,[42] solar cells,[43] batteries,[44] antimicrobial activity,[45] and water purification,[46] among others. Therefore, combining ALD and electrospinning enables the coating of fibers with specific functional materials (such as metallic oxides) at an atomic scale, the functionalization of nanostructures, the creation of controlled porous architectures, and the development of nanocomposites with enhanced properties.[40,47,48]

Among the many biopolymers suitable for electrospinning, lignin is emerging as a promising choice.[49,50] As the second most abundant natural polymer after cellulose, commonly found in plant cell walls, lignin offers strength and stiffness.[51] It is considered a by-product or residue from both the paper industry and the production of biofuels derived from lignocellulosic biomass.[52] The production of lignin nanofibers by electrospinning offers a promising opportunity to utilize biorefinery sidestreams and waste materials in new value-added applications.[53] This not only helps to reduce dependence on fossil fuels and mitigate deforestation but also promotes sustainability by closing the lifecycle of lignocellulosic components, thereby furthering the principles of circular economy.[54,55] Additionally, lignin exhibits significant advantages such as biodegradability, antioxidant properties, and antimicrobial activity, making it suitable for a wide range of environmental and health-related applications.[56–61] In particular, the biodegradability of gel-like fine dispersions of modified lignocellulosic waste materials in castor oil for lubricating purposes has been recently emphasized in comparison to traditional lubricating greases.[62]

However, lignin electrospinning poses a significant challenge due to its complex, random, and nonlinear structure and low molecular weight, making it difficult to achieve well-developed nanofiber mats. To overcome this challenge, the incorporation of a dopant polymer during the electrospinning process is essential.[35,49] This co-spinning polymer acts as a facilitator, increasing the entanglement density of lignin solutions and thereby improving their ability to form fibers.[35] The choice of a cellulose derivative as a dopant polymer in the electrospinning process offers numerous advantages due to its abundance, renewability, biocompatibility, and biodegradability.[63–65] In this regard, cellulose acetate butyrate (CAB) stands out as one of the most robust cellulose esters with favorable properties for electrospinning.[66] Moreover, due to the presence of acetyl and butyryl groups on the glucose unit, CAB exhibits a relatively hydrophobic character, which facilitates its dissolution in organic solvents.[67] CAB electrospinnability has been explored in previous studies.[66,68] In particular, Martin-Alfonso et al.[33] investigated the influence of CAB concentration in dimethylacetamide/acetone (DMAc/Ac) and methylene chloride/acetone (MC/Ac)-mixed solvents on its electrospinnability and found that the formation of bead-free nanofibers was favored at concentrations above 10 wt%, when solutions achieved extensional properties with relaxation times of at least 50 ms and shear-thinning flow behavior. Other works[69,70] reported the degree of compatibility between a commercial CAB and lignin esters with different moieties (acetate, butyrate, hexanoate, and laurate) and found that the blends of CAB and lignin esters exhibited strong phase interactions with a transition from full compatibility to semi-compatibility as the ester substituent increased from 2 to 12 carbon atoms. Whereas Dave et al.[69] studied the influence of lignin content on the properties of CAB solutions to evaluate the formation of fibers by a dry jet/wet spinning method.

Microfibers were successfully produced, and the mechanical properties of the fibers improved with the presence of lignin.

In this work, electrospun nanostructures based on alkaline kraft lignin (AKL) and CAB were evaluated as castor oil structuring agents, aiming to produce gel-like lubricants based on renewable components. For this purpose, the electrospinnability of AKL solutions doped with CAB was investigated, and different types of nanostructures were prepared by adjusting the solution concentration and AKL/CAB ratio. The physical and morphological properties of the electrospun AKL/CAB nanostructures were analyzed in relation to the physicochemical properties of the spinning solution. Furthermore, the rheological properties of fine dispersions of AKL/CAB nanofibers in castor oil were investigated and related with the characteristics of the electrospun membranes. Finally, for the first time, the tribological properties of the oleo-dispersions were tuned and remarkably improved by depositions of TiO_2 on AKL/CAB nanofibers using the ALD technique. These newly developed advanced oleo-dispersions are proposed as an efficient green alternative to traditional lubricating greases and also reveal a new avenue for lignin valorization, in line with the current environmental policies and circular economy principles.

2. Results and Discussion

2.1. Electrospinnability of AKL/CAB Solutions

Numerous studies have revealed a correlation between electrospinnability and the physicochemical properties of the spinning solutions, such as extensional and shear viscosities, surface tension, and electrical conductivity. These properties are influenced by the type of polymer, its molecular weight, the polymer–solvent interactions, and polymer solution concentration.[38,71,72] **Figure 1**a plots the viscous flow curves of several spinning solutions for different AKL/CAB concentrations and a selected 50:50 AKL:CAB weight ratio. All the spinning solutions showed Newtonian behavior over the range of shear rates analyzed, with the shear viscosity (η) increasing with the solution concentration, as reported elsewhere.[73] Figure 1b shows the specific viscosity, η_{sp} ($\eta_{sp} = (\eta/\eta_s) - 1$, where η_s is the solvent viscosity), versus concentration plot in log–log scales for AKL/CAB solutions. As well known, this plot allows the identification of transitions between concentration regimes and reveals, in this case, the critical entanglement concentration (C_e),[38,73] which delimits the semidilute non-entangled regime and the semidilute entangled domain, identified by a change in the slope of this graph.[38,74] The approximate value of C_e is 7.2 wt% and the scaling exponents obtained in both domains are $\eta_{sp} \approx C^{1.44}$, below C_e, and $\eta_{sp} \approx C^{3.64}$, above C_e, which are in agreement with the expected values for a neutral polymer in a good solvent.[75] C_e can be used as a reference to evaluate the electrospinnability of polymer solutions and the resulting morphology of the electrospun nanofibers. Several studies suggest that a concentration of around 2–2.5 times C_e is necessary to obtain homogeneous nanofiber mats.[38,76]

A hydrodynamic analysis was performed to improve the understanding of polymer–solvent interactions. The intrinsic viscosity, a parameter that reflects the ability of macromolecules to increase the solution viscosity without relying on intermolecular interactions, was evaluated using the well-known Kraemer

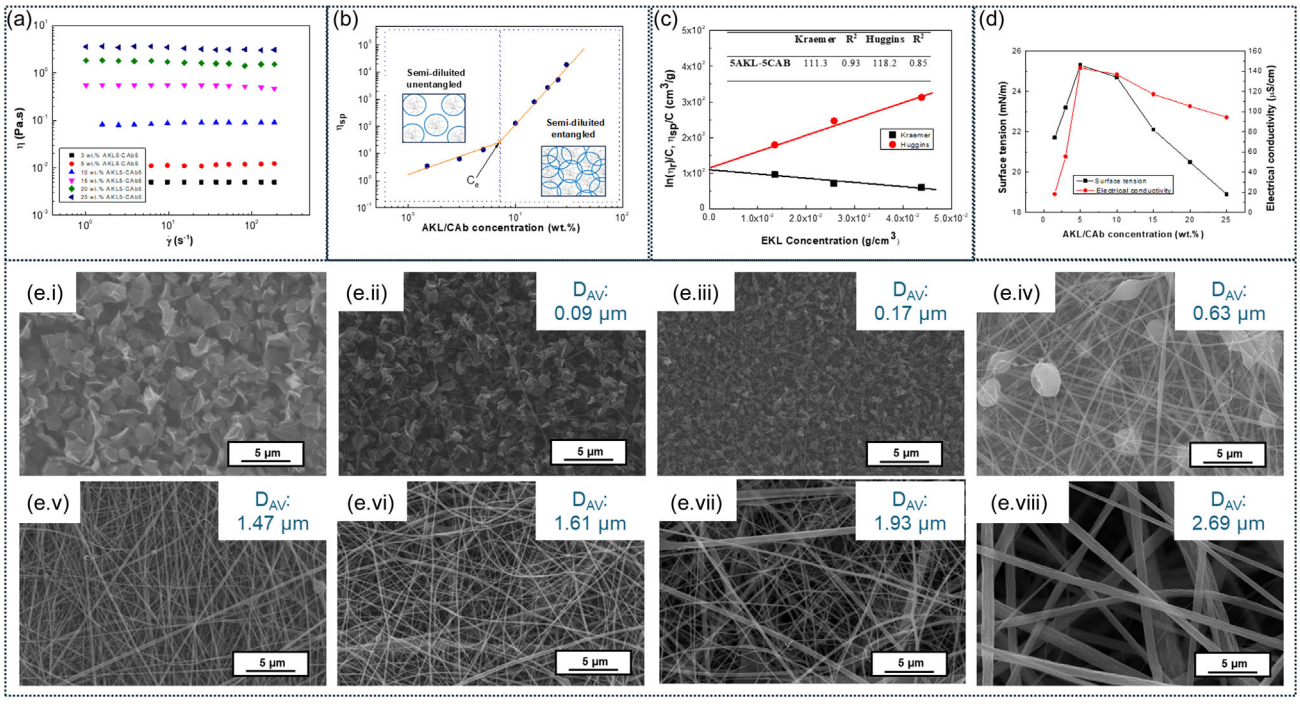

Figure 1. a) Viscous flow curves; b) specific viscosity versus concentration; c) Kraemer and Huggins models; and d) surface tension and electrical conductivity for 5AKL/5CAB spinning solutions at different concentrations in 1:2 DMF/Ac binary solvent; e) SEM images of electrospun nanostructures obtained from 5AKL/5CAB solutions at different concentrations: i) 1.5 wt%, ii) 3 wt%, iii) 5 wt%, iv) 7 wt%, v) 10 wt%, vi) 15 wt%, vii) 20 wt%, and viii) 25 wt%.

and Huggins relationships,[77] as shown in Figure 1c for solutions of AKL/CAB at 50:50 weight ratio. Both relationships provide intrinsic viscosity values of 111.3 and 118.2 $cm^3 g^{-1}$, respectively, calculated by extrapolation to obtain the Y-intercept value at zero concentration. This parameter provides valuable information about the interactions between the individual polymer molecules and the solvent, as well as the average specific hydrodynamic volume of the polymers or its average molecular weight,[78] considering a complex mixture of two polymers, in this case. According to de Gennes' restructuring theory,[79] a C_e value of ≈7.6 wt% was estimated from the intrinsic viscosity, which is in agreement with the empirical results shown in Figure 1b.

Figure 1d shows the evolution of electrical conductivity and surface tension of AKL/CAB solutions in the *N,N*-dimethylformamide (DMF)/acetone (Ac) (1:2) solvent mixture as a function of concentration. Both the surface tension and the electrical conductivity increase with the concentration of the spinning solution up to around 5 wt%, and after that they gradually decrease. This behavior is associated with the transition from an unentangled to an entangled semidilute regime. The decrease in electrical conductivity is due to the decrease in charge mobility caused by the reduced mobility of molecules in the semidilute entangled regime.[73] In contrast, the decrease in surface tension facilitates the electrospinning process by allowing the solution to stretch and form thinner fibers due to the reduction in cohesive forces. These results are consistent with those reported previously.[33,72]

Figure 1e shows scanning electron microscopy (SEM) micrographs of AKL/CAB electrospun nanostructures obtained from solutions of 50:50 AKL:CAB weight ratio at different concentrations. As can be observed, neither fibers nor interconnected bead–fiber structures were generated from a 1.5 wt% solution, essentially resulting in an electrospraying phenomenon instead of electrospinning and leading to the formation of agglomerated microparticles (see Figure 1ei). Similarly, morphologies predominantly consisting of micro- and nanometer-sized particles interconnected in this case by thin filaments with average diameters of 0.09 and 0.17 μm were obtained by slightly increasing the solution concentration to 3 and 5 wt%, respectively (Figure 1eii,iii), whereas a higher density of beaded nanofibers with average diameters of 0.63 and 1.47 μm was observed for 7 and 10 wt% spinning solutions, respectively (Figures 1eiv,v). Finally, when the concentration was increased above 10 wt%, homogeneous nanostructures entirely consisting of fibers were obtained, with an average diameter that increases with the solution concentration (Figure 1evi–viii). These results are in agreement with the hypothesis which suggests that above C_e, the electrospun mats exhibit morphologies predominantly formed by fibers. Furthermore, the results are consistent with the aforementioned previous studies that refer concentrations of 2–2.5 times C_e to obtain electrospun nanostructures formed by homogeneous fibers without bead defects.

2.2. Influence of the AKL/CAB Ratio on the Properties of Electrospun Nanostructures

Figure 2a shows SEM micrographs of the nanostructures obtained by electrospinning solutions with 25 wt% total polymer concentration at different AKL/CAB mass ratios. It is observed that solutions with high CAB contents produce uniform nanofibers with average fiber diameters (D_{AV}) of 1.93 and 1.71 μm (see Figure 2ai,ii). These morphologies are favored by the high proportion of a linear polymer such as CAB, also with a higher molecular weight than AKL, promoting more effective entanglement of the polymer chains in solution, and ultimately allowing for a more stable electrospinning process.[33,80] As the amount of AKL in the blend increases, a decrease in fiber diameter and an increase in structural heterogeneity were observed (Figure 2aiii), particularly evident in formulations with 8:2 and 9:1 AKL:CAB ratios (Figure 2aiv,v). Thus, morphologies such as micro- and nanoparticles associated with thin fibers are apparent. These results confirm the reduced ability of AKL to form continuous and steady electrospun jets, which is attributed to its highly heterogeneous and branched molecular structure that hinders the correct and stable formation of the Taylor cone.[81] In fact, electrospinning of solutions composed exclusively of AKL (100AKL) did not result in the formation of nanofibers, but rather in micrometer-sized electrosprayed particles (Figure 2avi). This behavior is in agreement with previous studies[38,73,82] indicating that low-molecular-weight polymers with a branched structure, such as AKL, fail to form fibers because they are not able to generate sufficient molecular entanglement in solution to stabilize the electrospinning process without the addition of a co-spinning or dopant polymer.[53,73] Authors such as Wu et al.[83] and Dallmeyer et al.[49] have documented that the addition of co-spinning polymers, acting as "carrier polymers", plays a key role to produce defect-free nanofibers. These findings underline the importance of adjusting the proportions of biopolymers according to their physicochemical properties to optimize the performance of the electrospinning process and the quality of the structures obtained.

In addition, Figure 2a shows the contact angle results embedded in the SEM images, which show that all the membranes present a hydrophobic character, attributable to the presence of CAB in the electrospun fibers. This hydrophobicity is mainly due to the chemical nature of this biopolymer, which is a cellulose derivative with a high degree of substitution of nonpolar acetyl and butyryl moieties (see Section "Materials"). A progressive decrease of this hydrophobic character was observed as the proportion of AKL in the AKL/CAB blend increased, which typically presents a high amount of phenolic and aliphatic hydroxyl groups.[84] As the AKL content increases, the higher presence of these polar groups on the surface of the fibers facilitates the formation of hydrogen bonds with water molecules, thus decreasing the contact angle and, therefore, the overall hydrophobicity of the system.

Figure 2b shows the thermogravimetric analysis (TGA) curves of AKL/CAB nanostructures with different AKL:CAB ratios. All samples exhibit one main degradation stage, with a maximum degradation rate at around 340 °C for all the samples studied. This is due to the fact that both AKL and CAB have very similar maximum degradation temperatures. However, the range of degradation for AKL is much broader than for CAB, as can be seen in Figure 2b. In this sense, nanostructures with high CBA proportions show slightly higher onset (T_{onset}) and maximum degradation rate (T_{max}) temperatures for this main degradation event (see Table S1, Supporting Information), as

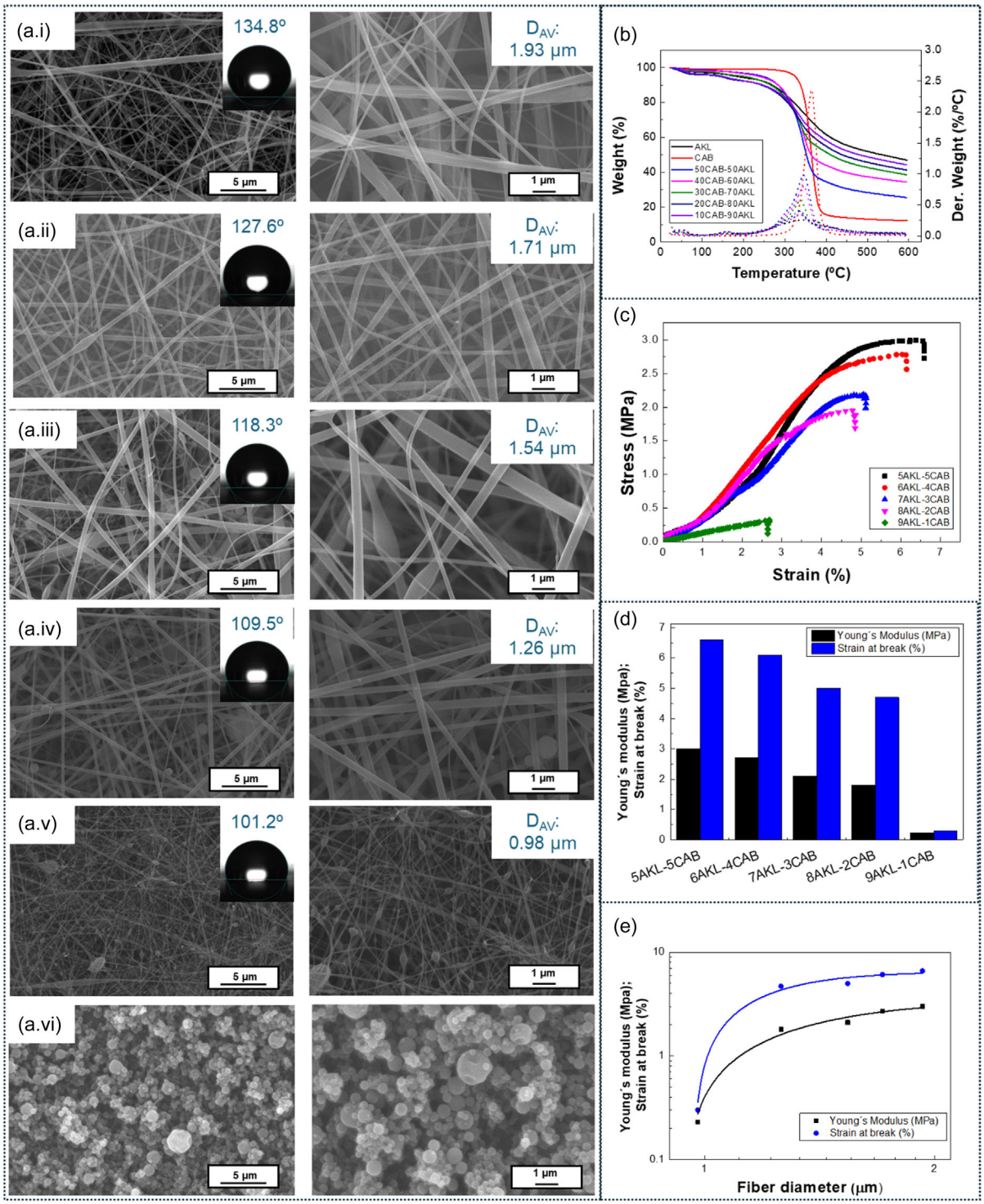

Figure 2. a) SEM images of electrospun nanostructures (solution concentration: 25% wt%) with embedded contact angle and fiber mean diameter data: i) 5AKL–5CAB, ii) 6AKL–4CAB, iii) 7AKL–3CAB, iv) 8AKL–2CAB, v) 9AKL–1CAB, and vi) 100AKL; b) TGA and c) DMA tension tests; d) values of Young's modulus and maximum strain at break; and e) empirical correlation of fiber diameter with Young's modulus and maximum strain at break of electrospun nanostructures with different AKL/CAB ratio.

well as lower amounts of final residue, i.e., 25.58 wt% for the 5AKL–5CAB sample versus 44.29 wt% for the 9AKL–1CAB sample.

Figure S1, Supporting Information, shows the spectra obtained by Raman, fourier transform infrared spectroscopy, and X-ray photoelectron spectroscopy (XPS) for the AKL/CAB

electrospun nanostructures with different AKL:CAB ratios. The results confirm that electrospun fibers are composed of both AKL and CAB biopolymers, while no new bands are observed, pointing out the absence of any chemical modification or interaction between AKL and CAB. These results suggest that the morphological and functional changes observed in electrospun nanostructures derived from AKL/CAB solutions are the result of physical interactions, without involving the formation of new chemical species detectable by the spectroscopic techniques used.

Figure 2c shows the stress–strain curves of electrospun nanofibers with different AKL:CAB ratios subjected to stretching. It is observed that formulations with higher CAB content, such as 5AKL–5CAB and 6AKL–4CAB, exhibit higher mechanical strength compared to those containing higher AKL:CAB ratios. Figure 2d shows the Young's modulus and strain at break values for the different formulations. The nanofibers containing higher amount of CAB present higher values of the Young's modulus, reflecting their higher stiffness. This is due to the linear nature of CAB, which provides structural cohesiveness and favors efficient interlacing of the polymer chains in the electrospinning process, which is reflected in both higher fiber diameters and a significant reduction of defects in the nanofiber mats. On the contrary, the branched molecular structure of AKL results in less stiff fibers.[35,73] Similarly, the strain at break decreases with increasing the AKL content. Fibers with a higher proportion of CAB are not only stiffer but also exhibit a higher elongation capacity before breaking, resulting in a significant improvement in the mechanical properties. This behavior indicates that CAB improves not only the strength but also the deformation capacity of the nanofibers, thus enhancing their mechanical performance, in agreement with its superior tensile properties.[85] It is worth noting that the resulting AKL nanostructure, i.e., sample 100AKL (Figure 2avi), does not elongate at all. Figure 2e relates the average diameter of the nanofibers with their mechanical properties, showing that both Young's modulus and strain at break increase exponentially with fiber diameter. In addition, the strain at break also increases with diameter, pointing out that thicker fibers have a greater capacity to absorb energy before breaking. This behavior is due to the fact that thicker fibers can better distribute stress throughout their structure, which delays mechanical failure. The exponential evolution observed in Figure 2e underlines the importance of controlling the fiber diameter, as this parameter seems to play a crucial role in the mechanical properties of nanofibers, despite other factors such as the reduction of defects also influence the tensile properties, as previously discussed.

2.3. Ability of AKL/CAB-Electrospun Nanostructures for Oil Structuring

Electrospun nanostructures, formed by meshes of well-defined nanofibers or, to a lesser extent, beaded nanofibers, are the only ones capable of producing stable gel-like systems once dispersed in castor oil.[35,73] In contrast, structures obtained by electrospraying, such as AKL100 (see Figure 2avi), produce unstable dispersions that lead to oil separation. This difference is attributed to the fact that nanofibers provide greater surface and aspect ratio for physical interactions that allow the oil to be trapped within the 3D network.[73] **Figure 3**a shows confocal microscopy images illustrating the morphological properties of the nanofibers once dispersed in the castor oil. It is evident that the fine dispersion of the nanofibers does not significantly alter their morphology. However, a noticeable swelling can be observed, yielding a significant increase in the diameter of both fibers and particles within the percolation network. This behavior becomes progressively more pronounced as the AKL:CAB ratio increases, as shown in Figure 3a.

Figure 3bi shows a 3D reconstruction of the oleo-dispersion prepared with a selected 5AKL–5CAB nanostructure (Figure 3ai) using confocal microscopy, whereas Figure 3bii shows the influence of this nanofiber concentration on the mechanical spectra of the oleo-dispersions obtained by small-amplitude oscillatory shear (SAOS) tests in the linear viscoelastic regime. As can be seen, the viscoelastic behavior is qualitatively similar regardless of the nanofiber loading. The observed viscoelastic behavior corresponds to a gel-like response, where the storage modulus (G') exceeds the loss modulus (G'') over the entire frequency range evaluated, with both moduli showing different trends depending on the frequency. G' shows a slight increase with frequency, while G'' reaches a distinct minimum. As can be seen, the values of G' and G'' increase with increasing nanofiber concentration, as a result of an increased fiber density within the percolation network.[73] However, the loss tangent, i.e., the ratio of G'' to G', is a unaffected by the nanofiber content, which therefore does not influence the relative elasticity of the oleo-dispersions.

Figure 3ci shows the variation of the SAOS functions at 25 °C for the oleo-dispersions prepared with nanostructures differing in the AKL:CAB mass ratio for a constant nanofiber content of 5 wt%. Again, the rheological response was qualitatively similar over the entire frequency range regardless of temperature and the AKL:CAB ratio. However, both G' and G'' decreased significantly with increasing the AKL proportion. This could be due to 1) an increase in the proportion of the component with lower average molecular weight (AKL) in the nanostructure, 2) its detrimental effect on the morphological properties, i.e., nanofibers with smaller diameters and less uniform (beaded fibers), and 3) eventually, lower mechanical properties of the electrospun nanostructures.[33,73,86] In contrast, increasing the temperature from 25 to 125 °C causes a gradual decrease in the values of the SAOS functions (see Figure S2, Supporting Information), which is an expected result previously reported for lubricating greases[87] and other oleo-dispersions.[30] More specifically, in the tests performed at 100 and 125 °C, the values of G' and G'' tend to approach each other, which indicate a transition to a more fluid behavior at higher temperatures. However, the decrease in SAOS functions with temperature is much lower than that previously reported for other oleo-dispersions.[30,88] For instance, Gallego et al.[30] who studied the influence of temperature on the SAOS functions of oleogels developed from different lignocellulosic pulps modified with hexamethylene diisocyanate, reported a dramatic decrease in the SAOS moduli (G' and G'') by approximately two decades at around 100 °C. However, this drastic softening has been overcome in the systems studied here.

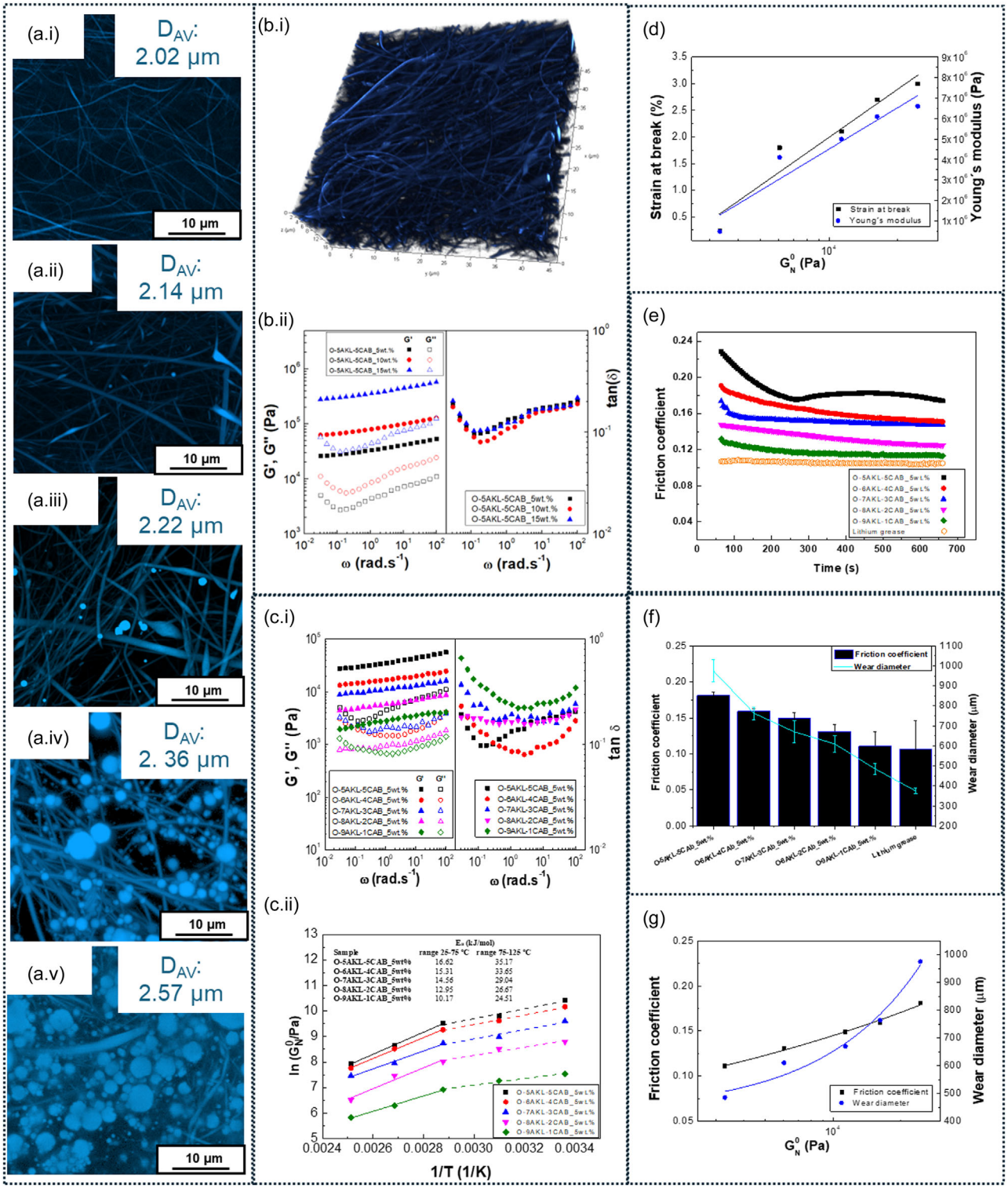

Figure 3. a) Confocal microscopy images of the oleo-dispersions prepared with different AKL/CAB ratios: i) 5AKL–5CAB, ii) 6AKL–4CAB, iii) 7AKL–3CAB, iv) 8AKL–2CAB, and v) 9AKL–1CAB; b) i) 3D reconstruction by confocal microscopy (5 wt% concentration), and ii) frequency-dependence of the storage (G') and loss (G'') moduli and loss tangent for oleo-dispersions formulated with 5AKL–5CAB nanostructure (5, 10, and 15 wt% concentrations); c) i) frequency dependence of the storage (G') and loss (G'') moduli and loss tangent for oleo-dispersions containing nanostructures with different AKL/CAB ratios (5 wt% concentration) and ii) evolution of G_N^0 with temperature in the form of Arrhenius' plot; d) empirical correlation between maximum strain at break and Young's modulus with G_N^0; e) evolution of the friction coefficient with time; f) histogram with tabulated values of friction coefficients and wear track diameter; and g) empirical correlation between the friction coefficient and the wear scar diameter with G_N^0 for oleo-dispersions prepared with nanostructures differing in the AKL:CAB ratio.

The influence of temperature on the linear viscoelasticity of the oleogels studied can be effectively visualized and quantified by plotting the plateau modulus (G_N^0), as defined elsewhere,[89] versus the reciprocal temperature (Figure 3cii). A slight change in the slope of the $\ln(G_N^0)$ versus $1/T$ plot was detected at around 75 °C, indicating a critical temperature beyond which the oleogels exhibit higher thermal susceptibility. To quantify this behavior, two distinct Arrhenius-type relationships were employed for the low- (25–75 °C) and high- (75–125 °C) temperature regimes:

$$G_N^0 = A \cdot e^{\frac{E_a}{R \cdot T}} \quad (1)$$

where E_a represents the activation energy (kJ mol^{-1}), which evaluates the thermal dependence, R is the universal gas constant (8.314 J mol^{-1} K^{-1}), T is the absolute temperature (K), and A is the pre-exponential factor (Pa). The E_a values obtained from the fitting are included in the table embedded within Figure 3cii. At lower temperatures (25–75 °C), the E_a values are relatively low, indicating low thermal susceptibility, while E_a values increase in the high-temperature range (75–125 °C). However, as previously mentioned, the thermal susceptibility of these oleo-dispersions at the high temperature range remains notably lower than that of oleogels prepared with chemically modified biopolymers.[30]

Aiming to illustrate the effect of the mechanical properties of the electrospun nanofibers on the viscoelastic response of the oleo-dispersions, the maximum strain at break and the Young's modulus of the nanofibers are plotted in Figure 3d as a function of G_N^0 of oleo-dispersions, evincing a linear correlation in both cases.

Finally, to assess the lubrication performance of these oleo-dispersions, Figure 3e collects the friction tests performed in a ball-on-three inclined plates steel–steel tribological contact, at constant normal load (20 N) and sliding velocity (10 rpm), using oleo-dispersions formulated with different AKL:CAB ratios at 5 wt% as lubricants. The friction coefficient progressively decreases with time until equilibration, suggesting the formation of a stable lubricant film.[90,91] Figure 3f presents the values of both the steady-state friction coefficient and the average diameter of the wear tracks generated on the steel plates. Oleo-dispersions formulated with electrospun nanofibers with higher CAB proportions exhibit larger wear tracks and friction coefficients. The system containing the AKL90–CAB10 nanostructure provided a remarkably low friction coefficient and reduced wear track size, similar to that found with the lithium grease used as benchmark. These results suggest that the more robust 3D nanofiber networks observed at higher CAB contents may hinder the oil release, which is not available to perform its lubricating function,[33,86] which is in agreement with the contact angle tests. In addition, as observed in Figure 3g, the softer gel-like rheological response of these oleo-dispersions may contribute to a better penetration of the nanofibers into the tribological contact zone. Thus, the friction coefficient increases linearly with G_N^0, while wear mark diameter increases exponentially.

2.4. Tuning the Tribological Properties of AKL/CAB Nanofiber-Based Oleo-Dispersions by Means of TiO_2 ALD

In previous sections, the oil structuring ability of electrospun AKL/CAB nanofibers has been demonstrated. However, only those with high AKL content exhibit tribological performance comparable to traditional lithium greases. In this section, the study has been focused on how the tribological properties can be tuned and remarkably improved by means of TiO_2 deposition on the nanofibers using the ALD technique. And, 9AKL–1CAB was chosen as a reference electrospun membrane since the derived oleo-dispersion produced with this nanostructure provided similar tribological performance than conventional lithium greases. **Figure 4**a shows images of TiO_2-deposited electrospun nanofibers after different ALD cycles obtained from SEM and energy dispersive X-ray (EDX) analysis. The ALD process was carried out by applying 1000, 1500, and 2000 cycles (denoted as 9AKL–1CAB_1, 9AKL–1CAB_1.5, and 9AKL–1CAB_2, respectively). ALD depositions were performed as detailed in Section "Preparation and Characterization of AKL/CAB-Electrospun Mats" to deposit a conformal and amorphous TiO_2 layer on the fibers and beads. Although the images do not allow direct observation of the nanometric thickness of the layers on the nanofibers, the analysis of the morphological uniformity in the SEM–EDX images (Figure 4a) confirms that the deposition was homogeneous over the entire surface of the fibers, regardless of the irregularities in the fiber morphology. This type of conformal coating is characteristic of the ALD process, which follows a self-controlled deposition model.[48,92] In this procedure, precursor molecules are chemically adsorbed on the surface of the substrate, the electrospun fibers in this case, and then react with the second precursor (H_2O) in a sequential process that allows layer-by-layer deposition.[93] The self-controlled nature of ALD ensures that each cycle uniformly covers the exposed surfaces, which is especially important in complex 3D structures such as the electrospun fiber mats.[47]

Figure 4b shows the EDX analysis of the electrospun 9AKL–1CAB fibers coated with 1500 cycles of TiO_2 ALD. The analysis points (001-005) indicated in the SEM image were selected according to their different morphological characteristics in terms of height (z-axis), geometry, and dimensions. The table shows the atomic percentages of oxygen (O), carbon (C), and titanium (Ti) for each of these points. The variations in Ti percentage (between 18.08% and 28.21%) are largely due to differences in the position of the points along the Z axis, as well as to their geometric characteristics. The spherical microparticles, due to their smaller surface area and their higher position on the z axis, have a lower amount of TiO_2 deposited. In contrast, nanofibers with a high surface to volume ratio allow a higher accumulation of TiO_2. This behavior is consistent with the physics of the ALD process, where conformal growth depends on surface accessibility. Locations with a larger surface area, such as nanofibers, tend to adsorb more precursors, while microparticles with a smaller surface area receive less material. Despite these local differences, the coating is globally rather homogeneous, as indicated by the standard deviation shown for the Ti content (±4.16%). This confirms the ability of ALD to provide uniform and controlled coverage, even in complex 3D systems where surfaces are at different heights and have significant geometric variations. In addition, Figure 4ai–aiii, which shows EDX images of electrospun 9AKL–1CAB fibers coated with TiO_2 after different numbers of ALD cycles, also displays the Ti content. A positive correlation between the Ti content and the number

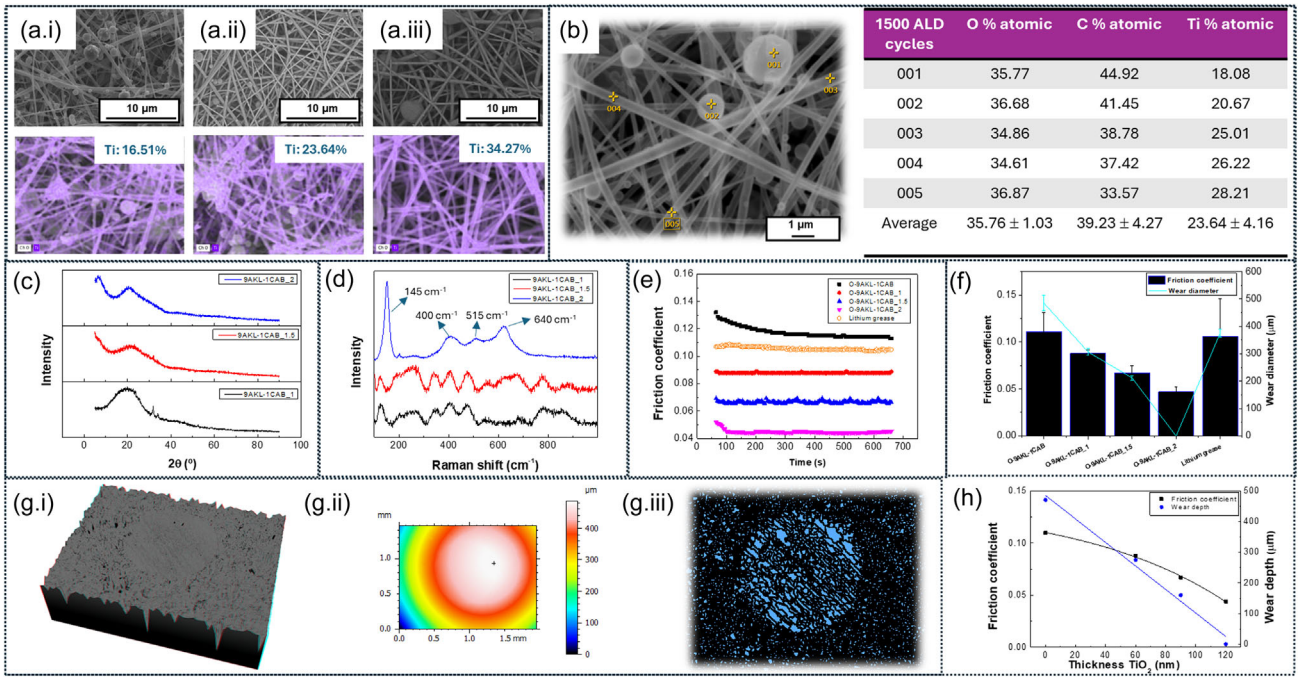

1500 ALD cycles	O % atomic	C % atomic	Ti % atomic
001	35.77	44.92	18.08
002	36.68	41.45	20.67
003	34.86	38.78	25.01
004	34.61	37.42	26.22
005	36.87	33.57	28.21
Average	35.76 ± 1.03	39.23 ± 4.27	23.64 ± 4.16

Figure 4. a) SEM–EDX images for the nanostructures prepared with different TiO_2 contents: i) 9AKL–1CAB_1, ii) 9AKL–1CAB_1.5, and iii) 9AKL–1CAB_2; b) SEM micrograph of 9AKL-1CAB_1.5 and spot EDX analysis on the electrospun mesh; c) XRD and d) Raman analysis for the nanostructures prepared with different TiO_2 concentrations; e) evolution of friction coefficient with time and f) histogram with tabulated values of friction coefficients and wear track diameter for the oleo-dispersions prepared with nanofiber mats having different TiO_2 contents; g) i) SEM analysis of wear volume, ii) depth, and iii) plastic deformation produced in the steel plate after the tribological test; and h) empirical correlation between the friction coefficient and the depth of the wear track with the thickness of the TiO_2 layer.

of cycles applied is observed. Thus, for the 9AKL–1CAB_1, 9AKL–1CAB_1.5, and 9AKL–1CAB_2 nanofiber mats, the average Ti contents are 16.51, 23.64, and 34.27%, respectively. The additional numbers of cycles facilitate a progressive accumulation of TiO_2, confirming the conformal nature of the ALD process and its ability to precisely modify surface properties.

Figure 4c shows the results of X-ray diffraction (XRD) analysis of electrospun 9AKL–1CAB membranes coated with different numbers of ALD cycles of TiO_2. The diffraction patterns show that the TiO_2 coating is predominantly amorphous, which can be deduced from the absence of sharp peaks, although small peaks at around 30°–35° can be visualized for 9AKL–1CAB_1 and 9AKL–1CAB_1.5 samples, probably due to the presence of small amounts of a crystalline rutile phase. This amorphous character is typical of TiO_2 deposited by ALD processes, where the physical principle favors growth of noncrystalline material over crystallization process, allowing a homogeneous distribution of the material on the surface of the electrospun fibers.[45,94] Figure 4d shows the spectra obtained by Raman spectroscopy. The peaks observed at around 145, 400, 515, and 640 cm^{-1} are characteristic of this amorphous phase of TiO_2,[95] confirming the successful deposition of the oxide onto the electrospun AKL/CAB fibers. The prominent peak at 145 cm^{-1} corresponds to the E_g vibrational mode, while the bands at 400 cm^{-1} (B_{1g} mode), 515 cm^{-1} (merged A_{1g} and B_{1g} modes), and 640 cm^{-1} (E_g) further support the presence of TiO_2. Furthermore, the increase in intensity of these bands with the increasing number of ALD cycles (see spectra for 9AKL–1CAB_2 sample) correlates with the amount of TiO_2 deposited, which is consistent with the results shown in Figure 4ai.

Figure 4e shows the evolution of the friction coefficient with time, determined in the tribological contact lubricated with oleo-dispersions prepared using electrospun 9AKL–1CAB membranes TiO_2-coated with different numbers of ALD cycles, in comparison with that obtained with a conventional lithium grease. The results show significant differences in the tribological behavior of the different systems studied. It is observed that the friction coefficient progressively decreases in all cases during the first few minutes until stabilization, suggesting the formation of an adequate lubricant film. The values of the friction coefficient and the average diameter of the wear marks are shown in Figure 4f. As can be seen, the oleo-dispersion based on 9AKL–1CAB_1 membrane shows a significant reduction in the friction coefficient compared to the TiO_2-free counterpart, as well as a lower friction coefficient and wear scar diameter than those obtained using the commercial grease. This beneficial effect is progressive as the number of ALD cycles is increased to 1500 and then to 2000 (oleo-dispersions of 9AKL–1CAB_1.5 and 9AKL–1CAB_2 nanofibers, respectively), with a further significant reduction in both the friction coefficient and wear size. It is worth noting that the AKL–1CAB_2 system totally prevents wear on the steel plates, definitely yielding a positive effect of TiO_2 deposition on the homogeneity of the electrospun nanofibers surface.

Figure 4gi shows a 3D reconstruction obtained using the backscattered electron detector (BSE) detector in topographic mode, where the wear volume generated by the steel ball on the plate using the TiO_2-free nanofiber-based (9AKL–1CAB_0) oleo-dispersion is observed. The wear volume can be analyzed by mapping the footprint depth, which reaches ≈500 μm (Figure 4gii). Wear involves plastic deformation, in the direction of the rotational movement, to some extent, as shown in Figure 4giii, which represents the domains of the grains making up the steel plate. Figure 4h plots the friction coefficient and the depth of the wear footprints generated using each of the oleo-dispersions with different deposited TiO_2 contents. The data show that the friction coefficient decreases exponentially with the increasing TiO_2 layer thickness, while the wear footprint depth follows a linear evolution. Overall, it is worth noting the tribological behavior imparted by the TiO_2-deposited fibers, since friction coefficients as low as those observed with the 9AKL–1CAB_2-based oleo-dispersion have not been previously reported for any semisolid lubricant, apart from totally preventing wear.

3. Conclusions

In this study, electrospun nanofibers based on AKL and CAB were successfully evaluated as renewable structuring agents for vegetable oils. In addition, deposition of TiO_2 layers on their surface conferred remarkable tribological properties to the resulting sustainable oleo-dispersions, which have great potential for replacing conventional lithium greases.

The electrospinnability of CAB-doped AKL solutions in a 2:1 v/v *N,N*-dimethylformamide/acetone solvent mixture depends on the solution concentration and the AKL:CAB ratio. Suitable electrospinnability and nanofiber-dominated morphologies were achieved at solutions concentrations above the critical entanglement concentration (C_e). Higher CAB contents in the AKL/CAB blend also improve electrospinnability promoting the formation of uniform and stable nanofibers. The average fiber diameter of electrospun nanofibers increases with the solution concentration and CAB proportion.

The elongational mechanical properties and the hydrophobic character of electrospun membranes were enhanced at higher CAB contents, whereas tribological properties once dispersed in castor oil improved with the AKL:CAB ratio. The improvements in the elongational mechanical properties are also related to the increased nanofiber average diameter. Therefore, a balance between AKL and CAB needs to be considered.

Electrospun nanostructures composed predominantly of nanofibers, or at least beaded nanofibers, produced stable gel-like oleo-dispersions in castor oil at different concentrations (5, 10, and 15 wt%). In contrast, nanostructures composed of particles, such as those obtained from CAB-free AKL solutions, resulted in unstable dispersions. The rheological properties of electrospun AKL/CAB nanofiber-based oleo-dispersions were significantly affected by both the AKL:CAB weight ratio and the nanofiber concentration, and correlated well with the mechanical properties of the electrospun membranes. Temperature caused a gradual and steady decrease of the viscoelastic functions but the drastic softening typically found in other oleo-dispersions and conventional greases at around 100–120 °C was overcome in these formulations.

Tribological studies indicated that oleo-dispersions of nanofibers with higher AKL contents provided lower friction coefficients and wear scar size. In particular, the 9AKL–1CAB electrospun membrane conferred lubrication properties very similar to those of conventional lithium greases. More remarkably, it was demonstrated that the tribological properties of electrospun AKL/CAB membranes can be effectively tuned and improved by TiO_2 atomic layer deposition. Increasing depositions of TiO_2 layers on AKL/CAB nanofibers lead to a significant reduction in the friction coefficient and an improvement in wear resistance compared to TiO_2-free samples and commercial lithium greases. This behavior is attributed to the ability of ALD to deposit conformal and homogeneous TiO_2 layers on the electrospun fibers, which favors the formation of a stable lubricating film with additional antifriction and anti-wear properties.

These results represent a significant advance in the field of lubrication and highlight the synergy between the ALD technique and the electrospinning of biopolymers to achieve a new generation of highly efficient, multifunctional, and renewable structurants for sustainable semisolid lubricant formulations.

4. Experimental Section

Materials: Commercial AKL and CAB ($M_n \approx 70\,000$, and $DS_{acetyl} = 12$–15 wt%, $DS_{butyryl} = 35$–39 wt%, and $DS_{hydroxyl} = 1.2$–2.2 wt%) were purchased from Merck Sigma-Aldrich and used as received. A comprehensive characterization of this commercial AKL (Product No. 370959), including molecular weight, hydroxyl content, and sulfur impurities, can be found elsewhere.[96] DMF (purity ≥99.8%) and acetone (Ac, purity ≥99.1%) were also purchased from Merck Sigma-Aldrich (Darmstadt, Germany) and used as solvents. Castor oil (Guinama, Valencia, Spain) was selected as the oil medium for the preparation of oleo-dispersions. The fatty acid composition and primary physical properties of this vegetable oil are described in detail in another publication.[97] A lithium multipurpose grease (NLGI Grade 2) marketed by Bellota (Spain) was used as benchmark.

Preparation and Characterization of AKL/CAB-Spun Solutions: AKL and AKL/CAB solutions were prepared by dissolving the biopolymers in a 1:2 (wt/wt) DMF: Ac-mixed solvent system to obtain spinning solutions with concentrations ranging from 1 to 30 wt%. In addition, solutions with different AKL:CAB ratios were prepared at a reference concentration, as shown in **Table 1**. The preparation protocol consisted of adding both biopolymers to the mixed solvent and stirring for 24 h at room temperature (23 ± 1 °C).

Table 1. Nomenclature used for the solutions prepared according to the AKL/CAB proportions (wt/wt).

Sample Code	AKL [wt%]	CAB [wt%]
AKL100	100	0
9AKL–1CAB	90	10
8AKL–2CAB	80	20
7AKL–3CAB	70	30
6AKL–4CAB	60	40
5AKL–5CAB	50	50

The physicochemical characterization of AKL and AKL/CAB spinning solutions included surface tension, electrical conductivity, and viscosity measurements performed at room temperature (23 ± 1 °C) in triplicate for each solution to ensure accuracy. Electrical conductivity measurements were performed using a GLP 31 conductivity meter (Crison, Spain) calibrated with KCl standard solutions in the appropriate concentration range. Surface tension measurements were performed using a Sigma 703D surface tensiometer (Biolin Scientific, China) with a platinum Wilhelmy plate. Shear viscosity was determined in an ARES controlled strain rheometer (Rheometric Scientific, UK) equipped with coaxial cylinders geometry in a 0.1–200 s^{-1} shear rate range.

Preparation and Characterization of AKL/CAB-Electrospun Mats: Electrospinning of AKL/CAB solutions was conducted in a DOXA Microfluidics (Spain) chamber. A syringe containing 10 mL of the spinning solution was utilized and connected to an infusion pump to maintain a flow rate of 0.6 mL h^{-1}. A horizontal setup was arranged, with a distance of 15 cm between the collection plate and the tip of the needle (21 G dimensions). Electrical connections were established between the collection plate, the capillary, and the high voltage power supply, generating a potential difference of 15–17 kV. Electrospinning parameters (voltage, flow rate, and tip-to-collector distance) were systematically optimized in this study, following a methodology similar to that previously reported.[98] All experiments were performed at room temperature (23 ± 1 °C) under nearly constant relative humidity ($45\% \pm 1\%$).

For a selected nanofiber membrane (9:1 AKL:CAB ratio), TiO_2 thin film deposition was performed using tetrakis(dimethylamino)titanium (TDMAT, purchased from Sigma Aldrich) as the titanium precursor and H_2O as the oxidizing agent in a Beneq TFS 200 reactor. The deposition was carried out in thermal atomic layer deposition (TALD) mode to ensure a uniform and conformal coating on the electrospun fibers. The ALD process was carried out with a Beneq TFS 200 reactor in TALD mode. TDMAT was heated to 75 °C in a stainless-steel cylinder to maintain sufficient vapor pressure, while high-purity nitrogen (N_2) was employed as the carrier and purge gas at a flow rate of 20 sccm, maintaining a reactor pressure of 30 Pa. The deposition temperature was set at 150 °C. The ALD pulse sequence consisted of a 0.15 s TDMAT pulse, followed by an 8 s purge, a 0.015 s H_2O pulse, and another 8 s purge to ensure complete precursor removal. TiO_2 coatings were deposited by applying 1000, 1500, and 2000 ALD cycles, systematically varying the film thickness on electrospun fibers. The growth per cycle for TiO_2, determined on a monocrystalline silicon witness wafer by SEM, ellipsometry, and atomic force microscopy was 0.6 Å (see Figure S3, Supporting Information). Although more variable and heterogeneous, the thickness of TiO_2 coatings on the nanofibers was assessed by means of transmission electron microscopy (TEM) observations, which was roughly in agreement with that measured on the silicon witness wafer (see Figure S4, Supporting Information).

The morphology of the electrospun mats was evaluated using field-emission SEM (FE-SEM, Hitachi High Tech, Japan), equipped with a secondary electron detector and an EDX detector model Ultim Max (Oxford Instruments PLC, UK), operating at an accelerating voltage of 15 kV. Due to the limited conductivity of the nanostructures, a gold coating was applied prior to imaging using a sputter coater (HHV, UK).[99] Occasionally, as aforementioned, to better evidence the fiber/TiO_2 interface and validate the thickness of TiO_2 coating, bright-field scanning transmission electron microscopy (BF-STEM) was also applied, at 30 kV and high vacuum mode, using the same FE-SEM microscope coupled with a BF-STEM detector. SEM and TEM images were analyzed using the open-source software FIJI (ImageJ) with the DiameterJ plugin,[100] developed specifically for this purpose. Water contact angle measurements were performed using the sessile drop method on an OCA 15 Plus goniometer (DataPhysics, Filderstadt, Germany). The surface tension of deionized (DI) water was first measured by the pendant drop method to ensure water purity, yielding an average value of 72.8 ± 0.22 mN m^{-1} (based on 10 measurements). For contact angle measurements, a 10 µL droplet of DI water was dispensed from a 0.52 mm diameter capillary and deposited onto the substrate. The contact angle was recorded immediately upon droplet deposition. TGA of kraft lignins and electrospun nanostructures was performed using a Q-50 analyzer (TA Instruments, New Castle, USA) under a nitrogen atmosphere. Samples (4–7 mg) were placed on platinum pans and heated from 25 to 600 °C at a rate of 10 °C min^{-1}. The weight loss was recorded to assess the thermal stability and decomposition of the materials. Crystalline structure analysis was conducted using XRD with a PANalytical Empyrean diffractometer, employing CuKα radiation ($\lambda = 1.5406$ Å). The scan was performed continuously from 10° to 90° (2θ) with a step size of 0.033°. The crystallite size was estimated using the Debye–Scherrer equation.[101] XPS was carried out using a Thermo Scientific Escalab 250Xi instrument, operating under ultrahigh vacuum conditions (≈10 mbar). The analysis utilized an Al Kα X-ray source ($h\nu = 1486.68$ eV), with the X-ray power set to 350 W and the voltage to 14 kV. Data was collected at a pass energy of 20 eV, with a spot size of 300 µm and an energy step size of 0.100 eV. Peak fitting was carried out using Voigt profiles in Thermo Avantage software (v5.41), with baseline correction applied using the Shirley–Sherwood method. Binding energies were calibrated to the C(1s) line at 284.8 eV. Raman spectroscopy was performed using a LabRAM HR Evolution spectrometer (Horiba, Japan), equipped with a 633 nm laser (nominal power of 17 mW). Spectra were collected under the following conditions: 100 s acquisition time, 10 accumulations, 50% laser power, a 600 g mm^{-1} grating, and a 100X long-working-distance objective. These settings were optimized to balance signal quality with minimal noise. Uniaxial tensile tests were performed using a dynamic mechanical analyzer (DMA Q800, TA Instruments, New Castle, DE) to evaluate the elongational mechanical properties of the electrospun mats. Samples were cut into strips (5.3 mm wide, 9.0–10.0 mm long, and 0.05 mm thick) and mounted using film tension clamps with a compliance of ≈0.17 µm N^{-1}. The width and thickness were measured with a standard electronic caliper (Fowler High Precision, Inc., Newton, MA), and the DMA instrument measured the initial sample length. Tensile tests were conducted at 23 °C in force-controlled mode, applying a preload of 0.01 N and a force ramp of 0.1 N min^{-1}.

Preparation and Characterization of Oleo-Dispersions: The electrospun nanostructures were gently removed from the collector plate using a pair of tweezers and a spatula. Typically, nanostructures were dispersed in castor oil at 5 wt% concentration. However, some selected membranes were dispersed at variable concentration (5, 10, and 15 wt%.). A mixer from IKA RW-20 (Germany), fitted with a low-shear anchor impeller, was utilized. The dispersion procedure was conducted delicately at a speed of 60 rpm for a duration of 24 h at room temperature. The resulting oleo-dispersions were then allowed to stand for another 24 h for subsequent characterization.

Rheological characterization of the oleo-dispersions was carried out in a controlled-stress Physica MCR-301 rheometer (Anton Paar, Austria) in a temperature range between 25 and 125 °C. SAOS tests were conducted within the linear viscoelastic range, covering frequencies from 0.03 to 100 rad s^{-1} under isothermal conditions using a rough plate–plate geometry (plate diameter: 25 mm, gap: 1 mm, relative roughness: 0.4). Tribological tests were performed using the same Physica MCR-301 rheometer equipped with a tribological cell. The setup consisted of a 1/2″ steel ball rotating against three 45° inclined rectangular steel plates, onto which the oleo-dispersions were tested as lubricants. The friction coefficient was determined under mixed lubrication conditions, maintaining a constant normal load of 20 N and a rotational speed of 50 rpm for 10 min. The wear scar diameter was assessed by SEM using an SEM model FlexSEM 1000 II (Hitachi, Tokyo, Japan) equipped with a BSE. The wear scars were further analyzed using Hitachi's 3DView software, providing a detailed characterization of the wear diameter, volume, and depth. Additionally, the morphology of the oleo-dispersions was evaluated using a Leica Stellaris 8 Falcon laser scanning confocal microscope. This system featured free spectral detection by AOBS (410–850 nm) and was equipped with Leica HCX PL APO lambda blue 63×/1.4 hybrid oil objectives and detectors.

Statistical Analysis: A statistical analysis was conducted on each of the chosen parameters. This analysis involved a one-factor analysis of variance, with three independent replications of each measurement. This approach allowed for the calculation of various statistical parameters,

including the mean and standard deviation. Furthermore, a test comparing means was executed to identify any significant differences ($p < 0.05$).

Supporting Information

Supporting Information is available from the Wiley Online Library or from the author.

Acknowledgements

This work is part of the Research Project PID2021-125637OB-I00, funded by MICIU/AEI/10.13039/501100011033 and by ERDF/EU. J.F. Rubio-Valle additionally received a Ph.D. Research Grant PRE2019-090632 from Spain's Ministry of Science and Innovation. The authors are grateful to Patricia Cerda, Alonso Concha, Luis Gerardo Silva, Lilia Bautista, Pedro Piza, Alberto Toxqui, and Nayely Pineda from CIMAV S.C., for their assistance in water contact angle, X-ray diffraction, XPS, Raman Spectroscopy, DMA, and SEM measurements. The authors also acknowledge on behalf of the iSensMEX collaboration (www.inaoep.mx/iSensMEX), a project supported by CONAHCYT (C-614/2021, Budget Program F003 "Platform for the development and manufacture of intelligent sensors and actuators applied in energy, health and security iSensMEX"). Funding for open access charge: Universidad de Huelva/CBUA. All funding is gratefully acknowledged.

Conflict of Interest

The authors declare no conflict of interest.

Author Contributions

José F. Rubio-Valle: conceptualization (equal); data curation (lead); formal analysis (equal); investigation (equal); methodology (equal); and writing—original draft (equal). **Eduardo Martínez-Guerra**: data curation (equal); investigation (equal); methodology (equal); and resources (equal). **Margarita Sánchez-Domínguez**: conceptualization (equal); formal analysis (equal); investigation (equal); resources (equal); and supervision (equal). **Elisa Vázquez-Lepe**: investigation (equal); resources (equal); and supervision (equal). **Ciro Rodríguez**: investigation (equal); resources (equal); and supervision (equal). **Concepción Valencia**: conceptualization (equal); formal analysis (equal); investigation (equal); methodology (equal); and supervision (equal). **José E. Martín-Alfonso**: conceptualization (equal); formal analysis (equal); investigation (equal); methodology (equal); supervision (equal); and writing—original draft (equal). **José M. Franco**: conceptualization (equal); formal analysis (equal); funding acquisition (lead); investigation (equal); methodology (equal); project administration (lead); resources (lead); supervision (equal); writing—original draft (equal); and writing—review and editing (equal).

Data Availability Statement

The data that support the findings of this study are available from the corresponding author upon reasonable request.

Keywords

atomic layer deposition, bio-based lubricating greases, electrospinning, nanocomposites, tribology

Received: February 27, 2025
Revised: April 21, 2025
Published online: May 15, 2025

[1] A. Sodiq, A. A. B. Baloch, S. A. Khan, N. Sezer, S. Mahmoud, M. Jama, A. Abdelaal, *J. Cleaner Prod.* **2019**, *227*, 972.
[2] S. Wichaisri, A. Sopadang, *Sustainable Dev.* **2018**, *26*, 1.
[3] E. B. Ali, V. P. Anufriev, B. Amfo, *Sci. Afr.* **2021**, *12*, e00756.
[4] A. K. Mohanty, S. Vivekanandhan, J.-M. Pin, M. Misra, *Science* **2018**, *362*, 536.
[5] T. Janković, A. J. J. Straathof, A. A. Kiss, *Front. Energy Res.* **2024**, *11*, 1340612.
[6] C. A. Wall-Markowski, A. Kicherer, P. Saling, *Environ. Prog.* **2004**, *23*, 329.
[7] A. Z. Syahir, N. W. M. Zulkifli, H. H. Masjuki, M. A. Kalam, A. Alabdulkarem, M. Gulzar, L. S. Khuong, M. H. Harith, *J. Cleaner Prod.* **2017**, *168*, 997.
[8] National Lubricating Grease Institute, *NLGI Lubricating Greases Guide*, 5th ed., Kansas City, MO **2006**.
[9] T. M. Panchal, A. Patel, D. D. Chauhan, M. Thomas, J. V. Patel, *Renewable Sustainable Energy Rev.* **2017**, *70*, 65.
[10] N. J. Fox, G. W. Stachowiak, *Tribol. Int.* **2007**, *40*, 1035.
[11] A. Hernández Battez, R. González, J. L. Viesca, J. E. Fernández, J. M. Díaz Fernández, A. Machado, R. Chou, J. Riba, *Wear* **2008**, *265*, 422.
[12] Z. Zhang, D. Simionesie, C. Schaschke, *Lubricants* **2014**, *2*, 44.
[13] A. Singh, P. Chauhan, T. G. Mamatha, *Mater. Today Proc.* **2020**, *25*, 586.
[14] X. Li, Y. Li, H. Yang, A. Liu, S. Zhang, L. Hu, *Tribol. Int.* **2025**, *205*, 110549.
[15] Y. Ren, X. Fan, K. Lin, S. Chen, M. Zhu, *J. Ind. Eng. Chem.* **2024**, *140*, 478.
[16] H. Wang, Y. Li, Q. Che, X. Liu, S. Zhang, H. Yang, L. Hu, *ACS Appl. Nano Mater.* **2025**, *8*, 2554.
[17] A. Saxena, D. Kumar, N. Tandon, T. Kaur, N. Singh, *Tribol. Lett.* **2022**, *70*, 108.
[18] Z. Wu, P. P. Thoresen, L. Matsakas, U. Rova, P. Christakopoulos, Y. Shi, *ACS Sustainable Chem. Eng.* **2023**, *11*, 12552.
[19] M. Trejo-Cáceres, M. C. Sánchez, J. E. Martín-Alfonso, *Cellulose* **2024**, *31*, 2063.
[20] D. F. Zambrano, J. G. González, C. Castillo, J. M. Henríquez, N. Parra-Muñoz, J. I. Urzúa, A. Rosenkranz, *Adv. Eng. Mater.* **2024**, 2401762.
[21] M. Toro-Gallego, C. Valencia, M. C. Sánchez, J. E. Martín-Alfonso, J. M. Franco, *J. Appl. Polym. Sci.* **2025**, *142*, e56489.
[22] A. Pires, G. Martinho, *Int. J. Life Cycle Assess.* **2013**, *18*, 102.
[23] P. Nowak, K. Kucharska, M. Kamiński, *Int. J. Environ. Res. Public Health* **2019**, *16*, 3002.
[24] R. Sánchez, G. B. Stringari, J. M. Franco, C. Valencia, C. Gallegos, *Carbohydr. Polym.* **2011**, *85*, 705.
[25] R. Gallego, J. F. Arteaga, C. Valencia, J. M. Franco, *Carbohydr. Polym.* **2013**, *98*, 152.
[26] M. Trejo-Cáceres, M. C. Sánchez, J. E. Martín-Alfonso, *Cellulose* **2024**, *21*, 2063.
[27] J. E. Martín Alfonso, R. Yañez, C. Valencia, J. M. Franco, M. J. Díaz, *Ind. Eng. Chem. Res.* **2009**, *48*, 6765.
[28] J. E. Martín-Alfonso, N. Núñez, C. Valencia, J. M. Franco, M. J. Díaz, *J. Ind. Eng. Chem.* **2011**, *17*, 818.
[29] R. Sánchez, G. Alonso, C. Valencia, J. M. Franco, *Chem. Eng. Res. Des.* **2015**, *100*, 170.
[30] R. Gallego, J. F. Arteaga, C. Valencia, M. J. Díaz, J. M. Franco, *ACS Sustainable Chem. Eng.* **2015**, *3*, 2130.
[31] C. J. Clarke, W.-C. Tu, O. Levers, A. Bröhl, J. P. Hallett, *Chem. Rev.* **2018**, *118*, 747.
[32] F. Valoppi, J. Schavikin, P. Lassila, I. Laidmäe, J. Heinämäki, S. Hietala, E. Haeggström, A. Salmi, *Food Struct.* **2023**, *37*, 100338.
[33] M. A. Martín-Alfonso, J. F. Rubio-Valle, J. E. Martín-Alfonso, J. M. Franco, *Adv. Sustainable Syst.* **2024**, *8*, 2300592.

[34] M. A. Martín-Alfonso, J. F. Rubio-Valle, J. P. Hinestroza, J. E. Martín-Alfonso, J. M. Franco, *Nano Mater. Sci.* **2025**, *7*, 90.
[35] J. F. Rubio-Valle, C. Valencia, M. Sánchez, J. E. Martín-Alfonso, J. M. Franco, *Cellulose* **2023**, *30*, 1553.
[36] J. L. Hernandez, M.-A. Doan, R. Stoddard, H. M. VanBenschoten, S.-T. Chien, I. T. Suydam, K. A. Woodrow, *Front. Biomater. Sci.* **2022**, *1*, 928537.
[37] K. Shi, K. P. Giapis, *ACS Appl. Energy Mater.* **2018**, *1*, 296.
[38] L. Kong, G. R. Ziegler, *Biomacromolecules* **2012**, *13*, 2247.
[39] G. K. Celep, K. Dincer, *Int. Polym. Process.* **2017**, *32*, 508.
[40] S. Vempati, K. S. Ranjith, F. Topuz, N. Biyikli, T. Uyar, *ACS Appl. Nano Mater.* **2020**, *3*, 6186.
[41] S. Sayegh, F. Tanos, A. Nada, G. Lesage, F. Zaviska, E. Petit, V. Rouessac, I. Iatsunskyi, E. Coy, R. Viter, D. Damberga, M. Weber, A. Razzouk, J. Stephan, M. Bechelany, *Dalt. Trans.* **2022**, *51*, 2674.
[42] O. Arslan, F. Topuz, H. Eren, N. Biyikli, T. Uyar, *New J. Chem.* **2017**, *41*, 4145.
[43] J. Li, X. Chen, W. Xu, C.-Y. Nam, Y. Shi, *Thin Solid Films* **2013**, *536*, 275.
[44] W.-H. Ryu, J.-W. Jung, K. Park, S.-J. Kim, I.-D. Kim, *Nanoscale* **2014**, *6*, 10975.
[45] C. López de Dicastillo, C. Patiño, M. J. Galotto, J. L. Palma, D. Alburquenque, J. Escrig, *Nanomaterials* **2018**, *8*, 128.
[46] W. Hao, C. Marichy, A. Brioude, *Environ. Sci. Nano* **2017**, *4*, 2311.
[47] J. Lee, I. S. Kim, M.-H. Hwang, K.-J. Chae, *Environ. Sci. Water Res. Technol.* **2020**, *6*, 1765.
[48] N. E. Richey, C. de Paula, S. F. Bent, *J. Chem. Phys.* **2020**, *152*, 040902.
[49] I. Dallmeyer, F. Ko, J. F. Kadla, *J. Wood Chem. Technol.* **2010**, *30*, 315.
[50] A. A. Adam, J. Ojur Dennis, Y. Al-Hadeethi, E. M. Mkawi, B. Abubakar Abdulkadir, F. Usman, Y. Mudassir Hassan, I. A. Wadi, M. Sani, *Polymers* **2020**, *12*, 2884.
[51] H. Lange, P. Giannì, C. Crestini, *Lignin Valorization: Emerging Approaches*, RSC, Cambridge **2018**, pp. 413–476.
[52] F. G. Calvo-Flores, J. A. Dobado, *ChemSusChem* **2010**, *3*, 1227.
[53] A. Raman, *J. Sib. Fed. Univ. Biol.* **2021**, *14*, 465.
[54] P. Morseletto, *Resour. Conserv. Recycl.* **2020**, *153*, 104553.
[55] S. Geisendorf, F. Pietrulla, *Thunderbird Int. Bus. Rev.* **2018**, *60*, 771.
[56] F. Luzi, W. Yang, P. Ma, L. Torre, D. Puglia, *Lignin-Based Materials for Biomedical Applications*, Elsevier, Amsterdam **2021**, pp. 291–326.
[57] D. Kai, L. P. Chow, X. J. Loh, *Functional Materials from Lignin*, World Scientific Publishing, Singapore **2018**, pp. 1–28.
[58] S.-L. Zou, L.-P. Xiao, W.-Z. Yin, T. Gui, Y. Zhang, Q. Li, R.-C. Sun, *Sustainable Mater. Technol.* **2024**, *39*, e00861.
[59] M. A. Jedrzejczyk, S. Van den Bosch, J. Van Aelst, K. Van Aelst, P. D. Kouris, M. Moalin, G. R. M. M. Haenen, M. D. Boot, E. J. M. Hensen, B. Lagrain, B. F. Sels, K. V. Bernaerts, *ACS Sustainable Chem. Eng.* **2021**, *9*, 12548.
[60] S. Camarero, M. J. Martínez, A. T. Martínez, *Biofuels, Bioprod. Biorefining* **2014**, *8*, 615.
[61] L. Cui, Z. Wang, Y. Zeng, N. Yang, M. Liu, Y. Zhao, Y. Zheng, *Fermentation* **2022**, *8*, 366.
[62] C. Fajardo, A. Blánquez, G. Domínguez, A. M. Borrero-López, C. Valencia, M. Hernández, M. E. Arias, J. Rodríguez, *Polymers* **2021**, *13*, 267.
[63] S. Kobayasi, K. Kashiwa, J. Shimada, T. Kawasaki, S.-I. Shoda, *Makromol. Chem., Macromol. Symp.* **1992**, *54–55*, 509.
[64] P. Wojciechowska, A. Heimowska, Z. Foltynowicz, M. Rutkowska, *PJCT* **2011**, *13*, 29.
[65] P. Kunthadong, R. Molloy, P. Worajittiphon, T. Leejarkpai, N. Kaabbuathong, W. Punyodom, *J. Polym. Environ.* **2015**, *23*, 107.
[66] H.-L. Tan, D. Kai, P. Pasbakhsh, S.-Y. Teow, Y.-Y. Lim, J. Pushpamalar, *Colloids Surf., B* **2020**, *188*, 110713.
[67] S. Zha, J. Yu, G. Zhang, N. Liu, R. Lee, *RSC Adv.* **2015**, *5*, 105692.
[68] P. Pascariu, L. Olaru, A. L. Matricala, N. Olaru, *Appl. Surf. Sci.* **2018**, *455*, 61.
[69] V. Davé, W. G. Glasser, *Polymer* **1997**, *38*, 2121.
[70] I. Ghosh, R. K. Jain, W. G. Glasser, *J. Appl. Polym. Sci.* **1999**, *74*, 448.
[71] J. F. Rubio-Valle, M. Jiménez-Rosado, V. Perez-Puyana, A. Guerrero, A. Romero, *Antimicrobial Textiles from Natural Resources*, Elsevier, Amsterdam **2021**, pp. 589–618.
[72] B. Veleirinho, M. F. Rei, J. A. Lopes da Silva, *J. Polym. Sci., Part B: Polym. Phys.* **2008**, *46*, 460.
[73] J. F. Rubio-Valle, C. Valencia, G. Ferraro, M. Carmen Sánchez, J. E. Martín-Alfonso, J. M. Franco, *J. Mol. Liq.* **2024**, *414*, 126248.
[74] H. Nie, A. He, J. Zheng, S. Xu, J. Li, C. C. Han, *Biomacromolecules* **2008**, *9*, 1362.
[75] A. V. Dobrynin, R. H. Colby, M. Rubinstein, *Macromolecules* **1995**, *28*, 1859.
[76] J. F. Rubio-Valle, C. Valencia, M. C. Sánchez-Carrillo, J. E. Martín-Alfonso, J. M. Franco, *ACS Sustainable Chem. Eng.* **2024**, *12*, 12260.
[77] A.-A. A. Abdel-Azim, A. M. Atta, M. S. Farahat, W. Y. Boutros, *Polymer* **1998**, *39*, 6827.
[78] A. Eich, B. A. Wolf, *ChemPhysChem* **2011**, *12*, 2786.
[79] W. Graessley, *Polymer* **1980**, *21*, 258.
[80] J. S. Gardner, J. O. Walker, J. D. Lamb, *J. Memb. Sci.* **2004**, *229*, 87.
[81] G. Gellerstedt, G. Henriksson, *Monomers, Polymers and Composites from Renewable Resources*, Elsevier, Amsterdam **2008**, pp. 201–224.
[82] S. L. Shenoy, W. D. Bates, H. L. Frisch, G. E. Wnek, *Polymer* **2005**, *46*, 3372.
[83] H. Wu, C. Liu, Z. Jiang, Z. Yang, X. Mao, L. Wei, R. Sun, *Text. Res. J.* **2022**, *92*, 456.
[84] X. Liu, Q. Liu, S. Wang, Z. Liu, G. Yang, H. Wang, W. Xiong, P. Li, F. Xu, Y. Xi, F. Kong, *Int. J. Biol. Macromol.* **2022**, *215*, 132.
[85] X. Wang, Y. Wang, Y. Xia, S. Huang, Y. Wang, Y. Qiu, *Text. Res. J.* **2018**, *88*, 1491.
[86] J. F. Rubio-Valle, C. Valencia, M. C. Sánchez, J. E. Martín-Alfonso, J. M. Franco, *Resour. Conserv. Recycl.* **2023**, *199*, 107261.
[87] M. A. Delgado, C. Valencia, M. C. Sánchez, J. M. Franco, C. Gallegos, *Tribol. Lett.* **2006**, *23*, 47.
[88] A. M. Borrero-López, F. J. Santiago-Medina, C. Valencia, M. E. Eugenio, R. Martin-Sampedro, J. M. Franco, *J. Renewable Mater.* **2018**, *6*, 347.
[89] J. D. Ferry, *Viscoelastic Properties of Polymers*, Wiley, New York **1980**.
[90] P. Wen, Y. Lei, Q. Yan, Y. Han, M. Fan, *ACS Appl. Mater. Interfaces* **2021**, *13*, 11524.
[91] P. Wu, X. Chen, C. Zhang, J. Zhang, J. Luo, J. Zhang, *Friction* **2021**, *9*, 143.
[92] J. Dendooven, C. Detavernier, *Atomic Layer Deposition in Energy Conversion Applications*, Wiley-VCH, New Jersey **2017**, pp. 1–41.
[93] H. Kim, H.-B.-R. Lee, W.-J. Maeng, *Thin Solid Films* **2009**, *517*, 2563.
[94] L. Avril, S. Reymond-Laruinaz, J. M. Decams, S. Bruyère, V. Potin, M. C. M. de Lucas, L. Imhoff, *Appl. Surf. Sci.* **2014**, *288*, 201.
[95] A. Bhatia, M. Hallot, C. Leviel, P. Roussel, J. Pereira-Ramos, C. Lethien, R. Baddour-Hadjean, *Adv. Mater. Interfaces* **2023**, *10*, 2202141.
[96] W. Zhao, L.-P. Xiao, G. Song, R.-C. Sun, L. He, S. Singh, B. A. Simmons, G. Cheng, *Green Chem.* **2017**, *19*, 3272.
[97] M. A. Martín-Alfonso, J. F. Rubio-Valle, G. M. Estrada-Villegas, M. Sánchez-Domínguez, J. E. Martín-Alfonso, *Gels* **2024**, *10*, 221.
[98] J. F. Rubio-Valle, C. Valencia, G. M. Estrada-Villegas, J. E. Martín-Alfonso, J. M. Franco, *Nanoscale* **2025**, *17*, 2728.
[99] Stokroos, Kalicharan, Van Der Want, Jongebloed, *J. Microsc.* **1998**, *189*, 79.
[100] N. A. Hotaling, K. Bharti, H. Kriel, C. G. Simon, *Biomaterials* **2015**, *61*, 327.
[101] U. Holzwarth, N. Gibson, *Nat. Nanotechnol.* **2011**, *6*, 534.